Characteristics of SnO_x films deposited by reactive-ion-assisted deposition

Seok-Kyun Song
SKION Corporation, 50 Harrison Street, Hoboken, New Jersey 07030
(Received 12 March 1999)

SnO_x films were deposited on glass, amorphous SiO_2/Si, and Si(100) substrates by oxygen ion-assisted deposition at various ion beam potentials (V_I) at room temperature and a working pressure of 8×10^{-5} Torr. The structural, chemical, and optical properties of the as-grown tin oxide films were investigated to determine the effects of the oxygen ion energy (E_{ave}) and ion/atom arrival ratio (R_i). X-ray diffraction (XRD) patterns indicated different growth directions with various E_{ave}. The as-grown films with oxygen/Sn ratio (N_O/N_{Sn}) of 2.03 and 2.02 had preferred orientation of (101) and (002), respectively. In addition, the as-grown film with low R_i was amorphous. Comparing the observed d spacings with those for standard SnO_2 samples, the as-grown films, which were crystalline had compressive and tensile stress depending on E_{ave}. The grain size increased from 7 to 11 nm with increasing ion beam potential for glass substrates. The crystalline grains were arranged in large spherical clusters. Such clusters play an important role in optical scattering. In transmission electron microscopy analysis, a buffer layer of amorphous tin oxide was observed at the interface between the substrate and the film, and the crystalline grains were grown on this buffer layer. The crystalline grains were arranged in large spherical clusters, and this shape directly affected surface roughness. Scanning electron microscopy images suggested that the small grain size and very dense grain structure might be due to the ion bombardment effects at the initial stage of film growth. Root mean square roughness values from atomic force microscopy showed that the surface roughness increased with increasing R_i, while the roughness decreased at $R_i = 1.39$ because the high bombarding ion energy broke the SnO_2 grains on the substrate, resulting in small grains. X-ray photoelectron spectroscopy peaks showed different N_O/N_{Sn} (1.51, 2.03, 2.02, and 1.96) for different values of R_i. Rutherford backscattering spectroscopy spectra showed that the tin-oxide thin films were inhomogeneous. The density of films decreased and the porosity and oxygen trapped in the films increased with increasing R_i. The densest film had about 6% porosity. The refractive index of films decreased with increase of the ion beam energy due to an increase in porosity. The degree of the dispersion of the refractive index and extinction coefficient decreased with increasing ion beam energy. A formula for the atomic elastic force was derived from the dispersion of the refractive index and d spacings derived from the XRD analysis. The atomic bonding force increased, and the stress of films was changed from compressive to tensile stress with increasing ion energy. [S0163-1829(99)03539-0]

I. INTRODUCTION

SnO_x thin films are particularly important for many device applications, such as in prototype gas sensors,[1] transparent conducting electrodes,[2] IR reflecting heat mirrors,[3] high-efficiency SnO_2/Si solar-cell devices,[4] and catalyses.[5] Tin-oxide thin films have been fabricated using many different techniques including spray pyrolysis of a solution of $SnCl_4$,[6,7] magnetic or RF sputtering,[8,9] ion beam sputtering,[10] the sol-gel method,[11] chemical vapor deposition,[12,13] and thermal evaporation.[14,15] However, such techniques have disadvantages such as relatively high deposition temperature and/or contamination. In the usual processes in depositing tin oxide, the films show defects due to oxygen deficiency, which affects the optical properties by causing an increase in the absorption coefficient and variations in the refractive index, as well as increasing the conductivity, oxidation catalysis and changing the electronic structure of SnO_2. For example, Cl contamination can lead to excessive conductivity and an increased extinction coefficient due to Cl scattering centers, in SnO_2 films deposited by chemical vapor deposition using $SnCl_4$ as a precursor. Therefore, the electro-optical properties of SnO_2 are strongly dependent on the chemical composition, microstructure, oxygen vacancies, and doping concentration of p- or n-type donors.[16,17]

Ion-assisted deposition (IAD) methods have many advantages, such as low-temperature film growth, smooth film surfaces, good control of crystallinity and composition, and fast nucleation of the material on the substrate.[18,19] IAD is especially useful for synthesizing oxide or nitride thin films because energetic gas particles can play both direct and indirect roles in film growth. Such the energetic ion bombardment can generate significant changes in crystal size and orientations, defect densities, electrical and optical properties, chemical stoichiometry, and surface morphologies.[20] Many dielectric films have been successfully deposited by IAD, but there have been only a few reports on the deposition and optical properties of tin-oxide films grown by reactive IAD (R-IAD) using oxygen. Also, there exists no general model to explain the effect of oxygen ion bombardment on tin-oxide film properties. If ion energy and ion flux are controlled, the microstructure of the film can be systematically studied.

SnO_2 crystallizes in the tetragonal rutile structure D_{4h}^{14} ($P4_2/mnm$) with two Sn and four oxygen per unit cell.[21] The lattice parameters are $a = b = 4.737$ Å, $c = 3.185$ Å and $c/a = 0.673$. Under typical deposition conditions, as-grown SnO_2 thin films are polycrystalline with the rutile

TABLE I. The experimental conditions for tin-oxide thin films deposited by R-IAD, and the calculated ions/atom arrival ratio and average energy/atom.

Samples	Ion beam potential (V) V_I	Ion current density (μA/cm^2) J	Deposition atom # $n(\times 10^{14})$	Ions/atom arrival ratio R_i	Energy/atom (eV/atom) E_{ave}	x of SnO_x in as-deposited films (from XPS) x
Film (*a*)	0	1.302	2.106	0.05	-	1.51
Film (*b*)	300	16.584	2.543	0.42	122	2.03
Film (*c*)	500	27.197	2.534	0.68	335	2.02
Film (*d*)	1000	54.789	2.484	1.39	1379	1.96

Formulas used for calculations.
$n = R \times 10^{16} / [71.5/\{(1+x)\times 2\}]$
$R_i = 6.25 \times 10^{18} \times J/n$
$E_{ave} = V_I \times 6.25 \times 10^{18} \times J/n$
Assume octahedral symmetry structure, $a = 4.737$, $c = 3.185$ Å, 6 atom/cell in structure→volume 71.5 Å.

structure.[22,23] Pure SnO_2 is an *n*-type semiconductor with a wide-band gap. Thin films deposited by various methods[24–26] have been found to have a direct optical band gap of 3.35–4.3 eV and a refractive index of 1.8–2.0. The chemiresistivity of SnO_2 films is determined by the chemisorption of hydroxide or oxygen ions on the surface, which can trap or scatter free carriers, generate potential barriers, or severely deplete the grains.[27]

In a previous article,[28] SnO_x thin films were fabricated by adjusting the relative arrival ratio of Sn metal to energetic oxygen ions at a fixed ion beam potential of 500 V, i.e., the average impinging energy of O_2^+ ions to SnO_x was controlled from zero to 100 eV/atom. The composition ratio of the films could be controlled, the refractive indexes decreased toward that of bulk (2.0), and the transmittance increased with increasing oxygen content by increase of the average arriving energy. However, SnO_2 thin films with stoichiometric composition were not fabricated and the crystallinity was not changed under these conditions. We had previously grown stoichiometric SnO_2 films by adjusting the oxygen ion energy.[29] We reported that the variation of the refractive index in stoichiometric tin-oxide films is due to the porosity of films. However, we could not obtain as-grown films with good crystallinity at a of working pressure of 1.5×10^{-4} Torr oxygen, so could not studied the relation optical properties with crystallinity of films.

In this work, we grew SnO_x thin films at working pressure 8×10^{-5} Torr by adjusting the oxygen ion energy from zero to 1000 eV at a fixed deposition rate of Sn metal and a constant discharge current for oxygen gas. Under these conditions, the amount of ionized oxygen was fixed during deposition, and thus it was expected that the relationship among the quality of grown film, the optical, the electrical characteristics, and energy of oxygen particles could be deduced. Another purpose of this study was to thoroughly investigate how to directly prepare thin SnO_2 films having different properties at room temperature without some other surface treatment. The optical properties related with the crystallinity, grain size, composition, and surface properties of those films are discussed.

II. EXPERIMENT

SnO_x thin films were deposited on BK7 glasses, SiO_2/Si (100) substrates, and Si (100) wafers at room temperature by adjusting the energy of oxygen ions. The SiO_2/Si substrates were formed by depositing a SiO_2 film with 300 nm thickness by the ion beam sputtering technique on the Si substrate at room temperature. The as-deposited SiO_2 films were amorphous, as confirmed by x-ray diffraction (XRD) and transmission electron microscopy (TEM). Surface roughness as measured by atomic force microscopy (AFM) was found to be 3.5 Å R_{ms}. The objective of this experiment was to investigate the possibility of preparing SnO_2 films having different structural properties without changing other experimental parameters and at lower pressure (8×10^{-5} Torr) than in our previous experiment (1.5×10^{-4} Torr).[29]

The R-IAD system for fabrication of tin-oxide films was shown in our previous paper.[29] The base pressure was 6×10^{-6} Torr and the deposition of tin-oxide films was carried out at an oxygen pressure of 8×10^{-5} Torr. Neutral Sn metal was evaporated by using a partially ionized beam source[19] at a rate of 0.3 Å/s and concurrently oxygen ions were assisted by using a 5-cm gridded cold hollow cathode ion gun. For IAD, oxygen was introduced into the discharge chamber of the cold hollow cathode ion gun at a flow rate of 6 ml/min, and the discharge current was fixed at 0.4 A, where the amount of ionized or activated oxygen was fixed. The ionized oxygen beam energy was controlled using an ion-beam potential (V_I) power supply from an oxygen gas gun, and V_I was varied from 0 to 1000 V during Sn metal evaporation. Even though when $V_I = 0$ V, the oxygen beam energy is about 30–40 eV lower slightly than the gas discharge voltage (40 V) in discharge chamber of gas gun because it is the potential difference caused by the discharge voltage and plasma density.[30,31]

The experimental conditions are listed in Table I. The arrival ratios (R_i) of ions to atom or the average energies (E_{ave}) transferred to the deposited SnO_x were calculated from the measured deposition rate and the ion current density. The calculation method was explained in our previous article.[29] In this experiment, stoichiometric and structural properties are reported to examine the effects on the film growth of variations in the average energy or of the relative arrival ratio of Sn metal to energetic oxygen ions.

The crystalline structures of the as-deposited SnO_x films were examined by XRD study using a Philips (PW 7602) diffractometer with Cu $K\alpha$ radiation at 30 mA and 40 kV.

Surface and interface microcrystalline structures of the films were investigated by TEM (JEM-2000EX, JEOL Co.) study using 200 kV. Surface and interface microstructures were examined by scanning electron microscopy (SEM) (Hitachi, S-4200FE). Examination of the surface topography of the films was carried out by AFM (Park Scientific, SFM-BD2). The surfaces were scanned at different 1×1 μm^2 areas more than 40 times and the root mean square of surface roughness (R_{ms}) was calculated automatically by a computer program. In order to determine the composition ratio and chemical state of the deposited SnO_x films, XPS analysis was performed with a Surface Scientific Instrument (model 2803-S) spectrometer having a base pressure of 2×10^{-10} Torr. XPS spectra were obtained using Al $K\alpha$ radiation ($h\nu = 1486.6$ eV), an x-ray monochromator using a quartz disperser, and a concentric hemispherical analyzer, with a maximum energy resolution of 0.48 eV. An Ar^+ sputter gun ($E_p = 4$ keV, with an emission current of roughly 5 mA) was used to remove a small amount of carbon contamination as well as a hydrated layer on the surface by sputtering for 60 s. The composition ratios and the chemical states were estimated by means of comparison of the deposited SnO_x films with a standard SnO_2 powder of known composition. Binding energies of Sn $3d$ and O $1s$ core level spectra were calibrated using the O $1s$ peaks at 284.6 eV. The composition and porosity of the films were investigated by Rutherford backscattering spectroscopy (RBS) employing $^4He^+$ ion accelerated by a Pelletron accelerator. The beam energy, current, and total dose were 2.000 MeV, 30 nA, and 10 μA, respectively. The samples were tilted 5° to the y axis for prevention of channeling effects. In order to investigate the optical constant (refractive index n, extinction coefficient k, and thickness of the films), the transmittances in the wavelength 200–1200 nm range were measured with a UV-Vis. Spectrophotometer (Perkin Elmer Lambda 19). The sheet resistivities were measured by the four-point probe method.

III. RESULTS AND DISCUSSION

A. Crystalline structure studies by XRD and TEM

Figures 1(a)–1(c) show x-ray diffraction spectra of tin-oxide thin films deposited on glasses, amorphous-SiO_2/Si, and Si substrates, respectively, which represent similar patterns for each substrate. The reason is that the surface of the substrates used in this study were amorphous, i.e., the SiO_2 film substrate is amorphous as demonstrated in the Experimental section, the silicon substrate has a native oxide layer, and the BK7 glass substrate is amorphous, also. But, the intensities of the peaks in the case of the glass substrates were weaker than those seen for SiO_2 film substrates and Si substrates.

The as-grown films prepared at 8×10^{-5} Torr oxygen pressure show a crystalline XRD peak, while the as-grown films prepared at oxygen pressure 1.5×10^{-4} Torr in our previous work[29] did not show a crystalline peak, although the other deposition conditions were the same. This result indicates the importance of working pressure. Since the mean free path at 8×10^{-5} Torr (63 cm) is longer than that at 1.5×10^{-4} Torr (45 cm), more of the energy of ion beam can transfer to the growing film, resulting in a crystalline film. The film (a) deposited at low energy (ions/atom arrival ratio $R_i = 0.05$) is amorphous, while the film (b) deposited at the relatively high energy of $E_{ave} = 122$ eV/atom ($R_i = 0.42$) is crystalline with a preferred (101) orientation and has also a small (110) peak. The (101) orientation is a stable low-energy face for SnO_2.[29] Films (c) and (d) deposited at higher energy $E_{ave} = 335$ eV/atom ($R_i = 0.68$) and $E_{ave} = 1379$ eV/atom ($R_i = 1.39$) exhibit crystallinity with highly preferred orientation along (002).

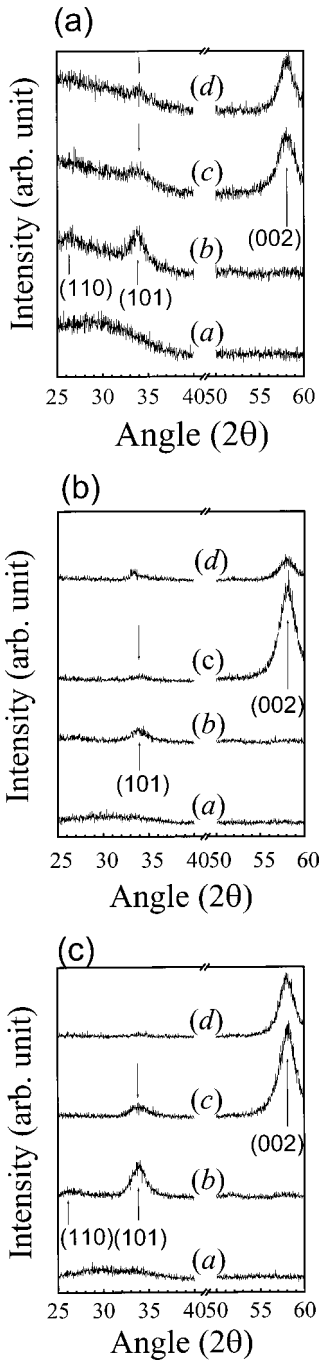

FIG. 1. X-ray diffraction patterns of tin oxide films deposited by oxygen ion beam assistance, for films on (a) glass, (b) SiO_2/Si, and (c) Si substrates, respectively.

The average grain size calculated by the Scherrer formula[32] from each peak is shown in Table II. In the case of the glass substrate, the grain sizes of films (b), (c), and (d) increased to 72, 95, and 108 Å with increasing the ion beam

TABLE II. Grain sizes calculated from XRD spectra for tin-oxide films on glass, SiO_2/Si, and Si substrate, and average surface roughness of tin-oxide films and the SiO_2/Si substrate.

Ion beam potential (V)	Grain size (Å)			Surface roughness R_{ms} (Å)
	Glass substrate	SiO_2/Si substrate	Si substrate	3.5 Å for SiO_2/Si substrate
0				8.3
300	71.6	92.0	101.5	19
500	95.0	92.4	98.7	43
1000	107.5	97.7	108.0	27

energy, respectively. In the case of the SiO_2/Si and Si substrates, the grain sizes of films (*b*) and (*c*) were similar, while that of the film (*d*) was larger. The effect of substrate difference with SiO_2/Si and Si substrate was not significant.

Figure 2 shows the *d* spacings calculated from the positions of the XRD peaks. According to the JCPDS 21-1250 card, the *d* spacings of the (101) and (002) planes of Cassiterite SnO_2 are 2.644 and 1.593 Å, respectively. The observed *d* spacings varied depending on the substrate. In the case of the glass substrate and the Si substrate, the *d* spacings of the (101) plane in the film (*b*) are 2.667 and 2.705 Å, which is larger than that of the literature sample. So, this film has a tensile stress perpendicular to the substrate. While the film (*c*) and (*d*) have a compressive stress along the *c* axis, they also have a tensile stress in the plane of the substrate. Since we observed an amorphous SnO_x buffer layer between substrate and film from cross-sectional high-resolution TEM (HTEM) results as shown in Fig. 3, the stress of the films is not likely to be due to mismatch with the substrate. We can assume that the incident ion energy is a more important parameter in determining stress than the effect of the substrate during the deposition process. The XRD results suggest that the energy of the incident ions has strong effects on the growth of preferred orientation films, and show that the growth plane was changed from (101) index being stable structurally at low ion energy to (002) index at high ion energy. These results agree with our previous report (the crystallinity shown after annealing process).[29]

Figure 3 shows photographs of electron diffraction patterns and cross-sectional HTEM images of tin oxide films on silicon substrates. Figure 3(a) (i) is a photograph of a cross-sectional diffraction pattern of film (*a*). The observed (110) pattern is very weak, so the film can be considered amorphous. This small difference of this observation from that of

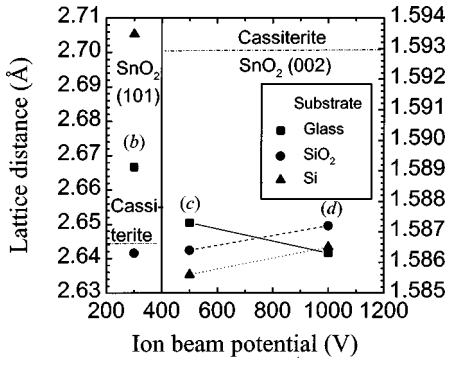

FIG. 2. Lattice distances calculated from XRD patterns of tin oxide films on glass, SiO_2/Si, and Si substrates.

the XRD pattern in Fig. 1(c) results from the fact that TEM analysis emphasizes short-range order as compared with XRD analysis.

In the photo (i) of Fig. 3(b) [the film (*b*)], the cross-sectional diffraction pattern shows an inside ring from the (110) plane and an outside ring from the (101) plane. Here, we wish to point out the difference between the plane index by cross-sectional diffraction pattern and the plane index by XRD analysis. The (101) plane grown parallel to the substrate (in XRD analysis) gives rise to the (101) and (200) index in cross-section (in the diffraction pattern analysis by TEM), the (002) plane appears as the diffraction patterns of (110), (200), and (210), and the (110) plane is observed as (110) and (002), respectively. Therefore, the film (*b*) in comparison with the XRD analysis is considered to have a polycrystalline structure with an inner ring (110) plane and an outer ring (101) plane. The photo (ii) shows a dark field image of the cross sectional TEM. The line pattern parallel to the substrate is observed, so we can assume that an inhomogeneous thin film was deposited. The photo (iii) shows a cross-section of the surface of film (*b*). The surface roughness seems to be in the few nm ranges. Lattice lines appear in position C in the photo (iii) and the angles of the lattice lines were found to be about 56° and 90°. Lattice lines of 56.07° and 90° correspond to a (101) plane in XRD analysis. Also, the (110) plane in XRD analysis is observed as lattice lines of 45° and 0°. The size of crystallite with the lattice line pattern is measured to be about 10 nm; this size is very similar to the grain size (Table II) obtained by using the Scherrer formula in XRD analysis. The capital *M* is a Moire pattern, which occurs when the lattice rotates or the lattice distances between two crystallites are similar to or multiples of each other.[33] Such Moire patterns were observed many times all over film (*b*). Crystalline defects such as dislocations and stacking faults are not observed in the crystal structure. Crystals with different orientations were found clustered in flowerlike masses[5] (position *F*), which is consistent with the observation of grains of a few tens nm size observed by SEM analysis in Fig. 4. We observed an amorphous phase in grain boundaries and between massed clusters. The photo (iv) is a cross-sectional HTEM image of an interface between the silicon substrate and a deposited thin film. A native oxide layer of about 8 nm thickness on the silicon substrate is observed in the interface. The *A* in photo (iv) is an amorphous tin oxide located on the native silicon oxide layer. *B* is a lattice line pattern with a 45° angle, which is identified as the (110) plane as observed in XRD analysis.

In the photo (i) in Fig. 3(c) [the film (*c*)], the bright hexagonal shape is a pattern of the silicon substrate, and the dim

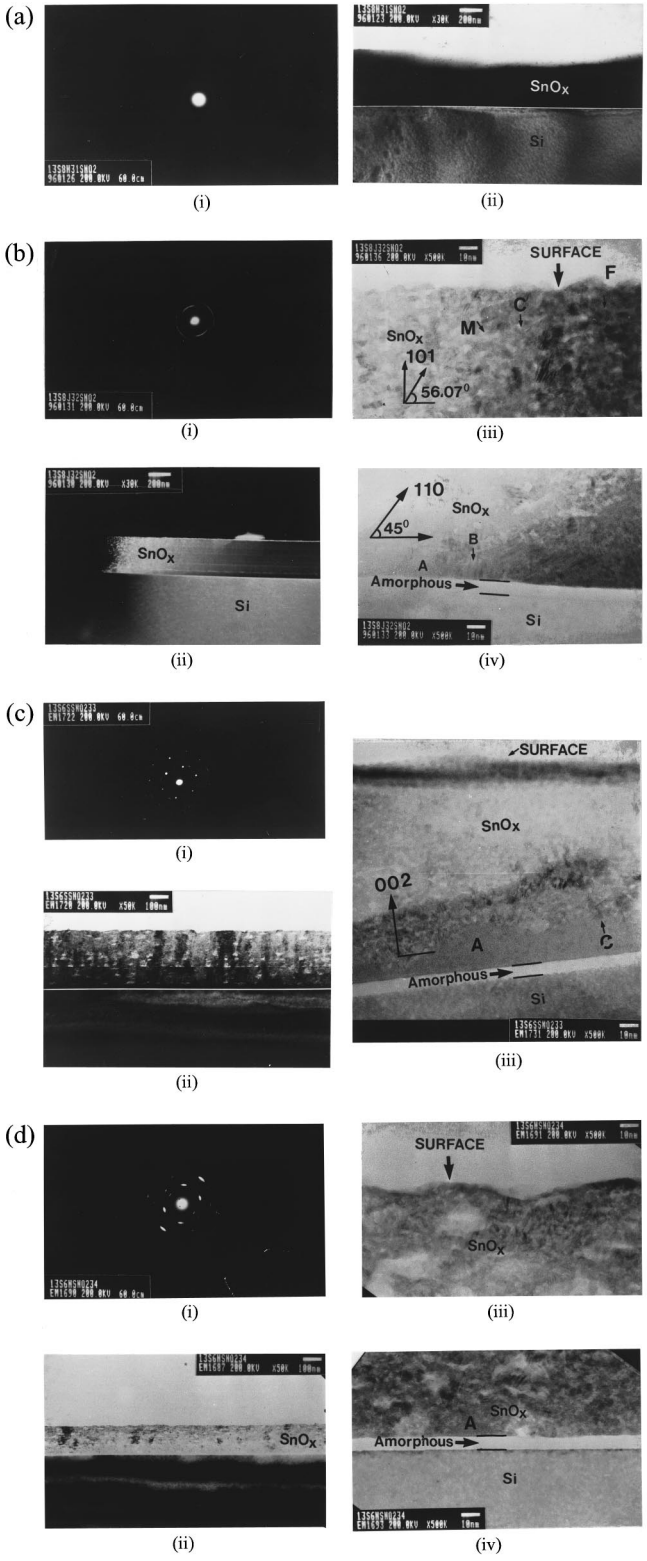

FIG. 3. HTEM photographs of images and electron diffraction patterns of cross-sectional view of tin-oxide films on Si substrates.

inner and outer points are diffraction patterns of (101) and (220) planes, respectively, from the tin oxide film. As already mentioned above, the former and latter correspond to the (101) and (002) peaks in XRD. The photo (ii) is a bright-field image of the cross-section, which shows that the film is inhomogeneous because the line pattern parallel to the substrate is like that in film (*b*). The photo (iii) shows a surface

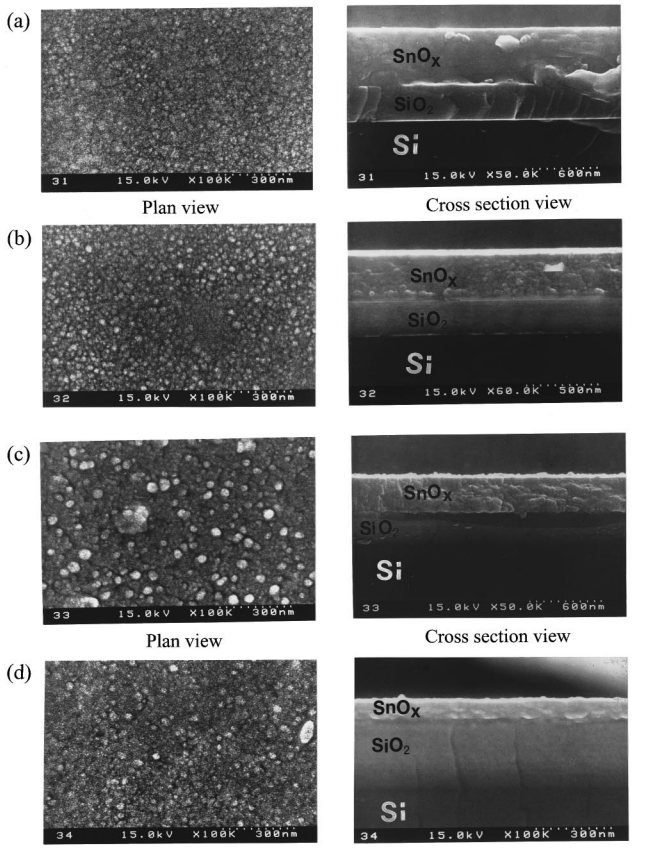

FIG. 4. SEM photographs of plan and cross-sectional view of tin-oxide films on SiO_2/Si substrates.

and an interface cross-section between the tin oxide film and the silicon substrate. An amorphous native silicon oxide layer is located at the interface, followed by an amorphous tin oxide layer of about 6-25 nm thickness, and finally the crystallized tin oxide film. The Moire patterns have smaller size and are fewer in number than those for film (*b*). The lattice line patterns with 56° is seen. Lattice lines vertical to substrate as shown in the position C correspond to the (002) plane in XRD analysis and appear more prominently than for film (*b*). This result is consistent with the results of XRD pattern (*c*) in Fig. 1(c). Namely, it means that crystallite are oriented with the (002) plane in the plane of the film more than for other orientations.

In the photo (i) in Fig. 3(d) [the film (*d*)], the brightly spread points close to the center are diffracted from the (101) plane, and the outer points are diffracted from the (220) plane. These points correspond to the (101) and (002) planes in the XRD analysis, respectively. From this diffraction pattern, it can be seen that the film is more highly crystallized than film (*c*). The peak intensity of the XRD pattern (*d*) in Fig. 1(c) is lower than that of pattern (*c*), which due to lower thickness rather than incomplete crystallization. The photo (ii) is a bright field image. This film shows evidence of inhomogeneity. In photo (iii), surface roughness is a few tens of nm, and the morphology slows slope. Moire patterns in the photo (iv) are very similar to that in the photo (iii) but are more numerous.

Whole the TEM analysis shows that an amorphous tin oxide was grown at first, then crystalline material was

formed mingled with an amorphous phase. The films were inhomogeneous. The crystallinity of the films increased with ion beam energy.

B. Microstructure and topography studies by SEM and AFM

Figure 4 shows SEM photographs of the cross-section and surface fine structure view of tin oxide films deposited on SiO_2/Si substrates. In Fig. 4(a) [film (*a*)], the grain boundaries in the surface and the cross-sectional view are indistinct. These results are consistent with the amorphous XRD pattern shown in Fig. 1(b). The surface fine structure in photograph (b) shows a uniform distribution of spherical grains with maximum size of 30 nm. In the cross-sectional view, columnar structures and voids, which are usually observed for other deposition methods, were not observed for our films. This means that the as-grown films prepared by IAD have a very dense structure and high packing density. The grain structure in the surface view in photograph (c) shows clusters of fine grains about 50 nm in size. Those clusters increased the surface roughness. However, the cross-sectional view shows that the massed clusters include many small size grains. This feature is consistent with the image of flowerlike polycrystalline clusters as shown in position *F* in Fig. 3(b). Especially, due to the masses that are exposed at surface, the surface roughness appears large. In photograph (d), the surface image clearly shows very small grains that are combined in big masses about 25 nm in size. In cross-sectional image, the aspect ratio of the bigger masses is about 3:1 with the long axis length 60–90 nm, which means that the film grows parallel to substrate. This spherical grain growth agrees with other results.[25,34] This small grain size might be due to the bombarding effects of the incident ion beam. The bombardment by the energetic oxygen ion beam could transfer its energy to the depositing Sn metal. This energy transfer increases the mobility of Sn, which increases nucleation density during the initial growth. In addition, we can assume due to the increased spatial density of nuclei from the small grains that this ion bombarding might break the bigger clusters.[35]

Figure 5 shows three-dimensional images of the surface morphology of tin oxide films. The surface roughness increased with ion beam energy, and the surface morphology was consistent with the SEM image in Fig. 4. The root mean square roughness (R_{ms}) as a function of ion beam potential is shown in Table II. The surface roughness of the bare SiO_2/Si substrate was 3.5 Å and the R_{ms} changed from 8.3 to 43 Å with increasing ion beam potential. When compared to the SEM image in Fig. 4, the change of surface roughness depends more on the size of massed clusters than on the grain size. From the film (*a*) to (*c*), the grain size increased with increasing average energy due to increasing surface diffusion. In film (*d*), the grain size became smaller (27 Å) because the average energy (E_{ave}=1379 eV/atom) is very large compared to the others that broke the massed clusters.[35] Also, as mentioned in the discussion of the SEM image, the surface roughness decreases by effect of the resputtering process, which might serve to preferentially resputter the projecting part of the films.

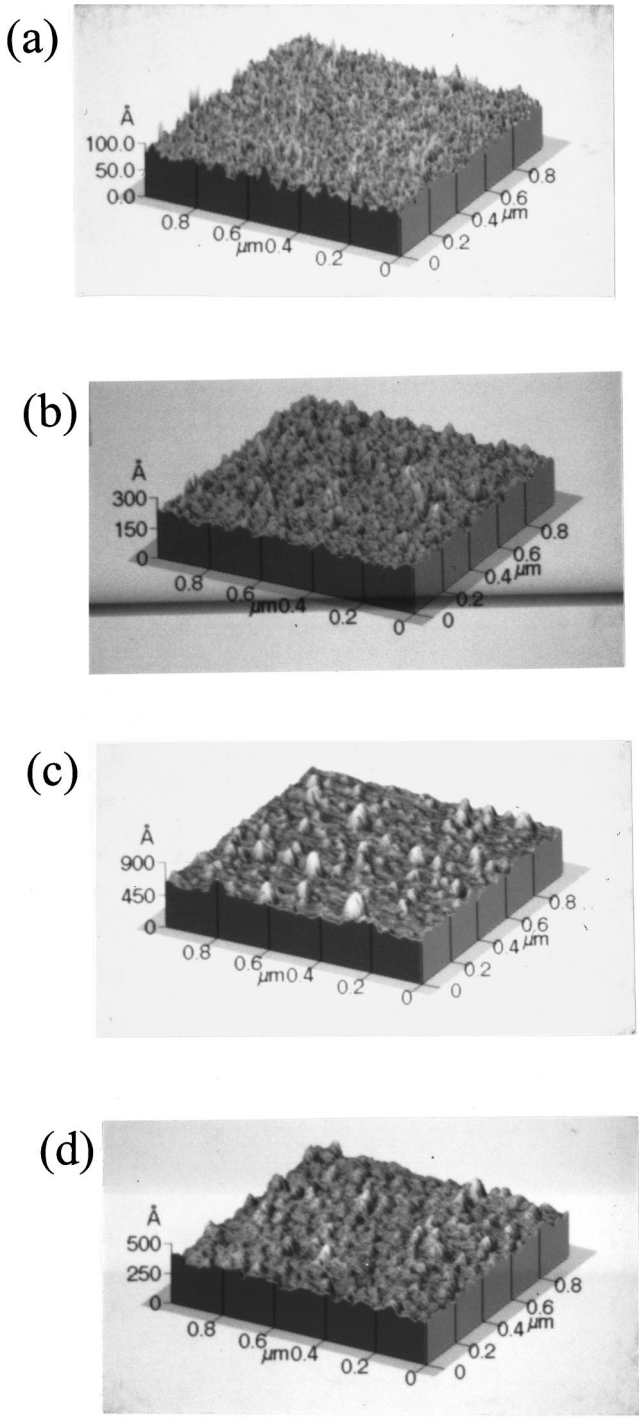

FIG. 5. Three-dimensional AFM images of tin-oxide films on SiO_2/Si substrates.

C. Composition and chemical characteristics studies by XPS and RBS

The high-resolution XPS spectra of Sn $3d_{5/2}$, Sn $3d_{3/2}$ core level, and O $1s$ for the as-grown films and standard SnO_2 powder are shown in Fig. 6. The binding energy (BE) of Sn $3d$ and O $1s$, and the atomic ratio (N_O/N_{Sn}) calculated from the XPS spectra, are listed in Table III. The standard SnO_2 powder has a Sn^{4+} state only, and the binding energy and the full width half at maximum (FWHM) of Sn $3d_{5/2}$ are measured to be 486.34 and 1.96 eV, respectively. In the film (*a*), the binding energy of $3d_{5/2}$ is observed at 485.99 eV and

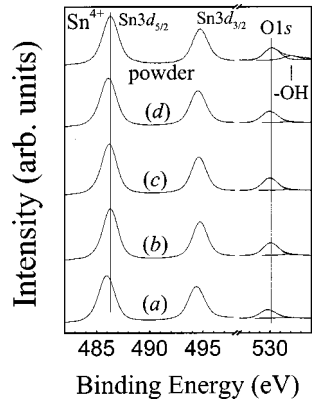

FIG. 6. X-ray photoelectron spectra of Sn $3d$ and O $1s$ core levels for tin-oxide films by R-IAD, and standard sample SnO_2 powder.

the peak position is slightly shifted to 0.35 eV lower energy than for that of the standard sample. This shift is smaller than the previous reported[28] 1 ± 0.02 eV binding energy difference between SnO_2 and SnO, and 0.5 eV reported by Ansell *et al.*[36] The atomic ratio of this film was calculated to be 1.51. Therefore, film (*a*) seems to be a mixed phase of SnO and SnO_2 grown at low average energy ($Ri = 0.05$). Films (*b*) and (*c*) have almost the same value of $3d_{5/2}$ binding energy as the standard sample, and accordingly, the calculated atomic ratio is 2.0. This means that stoichiometric films were grown. A distinct relationship between crystallinity by XRD and FWHM by XPS was not observed in this study. The crystallinity might be related with the core level state of Sn. Since the FWHM of the film (*b*) and (*c*) are 1.83 and 1.85 eV, smaller than the value of 1.96 eV of the standard sample, respectively, both films seem to have lower defect density than that of the standard sample. In film (*d*), the $3d_{5/2}$ binding energy is 486.17 eV, in the middle value between the film (*a*) and the standard sample, and the atomic ratio is calculated to 1.96. Accordingly, the film (*d*) seems to have SnO_2 as the main phase with a slight amount of SnO. Even though the average energy is higher than that of films (*b*) and (*c*), the composition is nonstoichiometric, which is due to preferential sputtering of oxygen as compared to Sn metal.[37,38]

The O $1s$ spectra in Fig. 6 show two components, a main peak at BE=530.2 eV and a broad small peak at BE=532 eV, attributed to oxygen in an oxide state and to adsorbed water or oxygen, respectively.[39] The hydration-related peak could not be completely removed by sputtering for 60 s using an Ar^+-ion gun. The position of the major O $1s$ peak changed from 529.82 eV [film (*a*)] to 530.10 eV [film (*b*)] with increase of the N_O/N_{Sn} ratio. The O $1s$ binding energy in film (*a*) appeared very similar to that seen for SnO. However, the oxygen binding energies of the other films were very close to those of SnO_2.

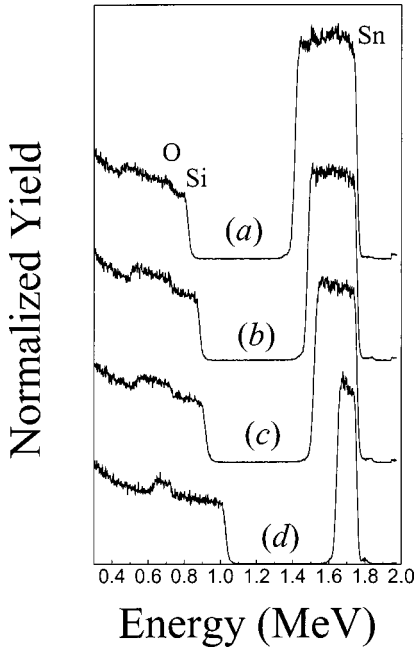

FIG. 7. Rutherford backscattering spectroscopy spectra of tin-oxide films grown on Si substrates.

RBS depth profiles of the tin oxide films are shown in Fig. 7. No impurities were observed in the tin oxide films; the only elements detected were Sn and oxygen. The interfaces between the films and the Si substrates are very clean, agreeing with the TEM results. From the spectrum of film (*a*), it appears that there are some layers that have a different composition; the composition ratio decreased near the surface. At the surface, a lot of oxygen is observed. In the spectrum of film (*b*), It appears that the composition ratio decreased slightly as the surface is approached, and there are some fine layers of different compositions which correspond to the layers observed in (ii) of TEM image (*b*). From the spectrum of film (*c*), Sn is observed to be distributed evenly. The middle layer shown in (ii) of TEM (*c*) can be distinguished in the oxygen RBS spectrum, with a higher oxygen content on the surface side than on the substrate side. The spectrum of film (*d*) is divided in two layers. The Sn concentration decreased

TABLE III. Binding energies of Sn $3d$ and O $1s$ core-levels of standard tin oxide powder and tin oxide thin films deposited by R-IAD, and the oxygen/Sn metal ratio calculated from XPS spectra.

Samples	Sn $3d_{5/2}$ (eV)	FWHM of Sn $3d_{5/2}$ (eV)	O $1s$ (eV)	FWHM of O $1s$ (eV)	N_O/N_{Sn}
Film (*a*)	485.99	1.93	529.82	1.82	1.51
Film (*b*)	486.36	1.83	530.10	1.74	2.03
Film (*c*)	486.26	1.85	530.00	1.74	2.02
Film (*d*)	486.17	1.95	529.99	1.86	1.96
SnO_2 powder	486.34	1.96	530.21	1.74	2.00

TABLE IV. The composition ratio, atom number/cm^3, porosity, and refractivity index calculated from RBS and spectrophotometric data.

Samples	RBS			Spectrophotometer	
	N_O/N_{Sn}	$N(\times 10^{22}\,\#/cm^3)$	P (%)	n (at 632.8 nm)	P (%)
Film (*a*)	1.69			2.1980	
Film (*b*)	2.70	7.917	5.67	1.9972	5.58
Film (*c*)	2.86	7.145	14.85	1.8739	20.67
Film (*d*)	2.95	5.870	30.04	1.8359	25.12

*The N of SnO_2 bulk is $8.3916\times 10^{22}\,\#/cm^3$, Density$=6.99\,g/cm^3$.

gradually approaching the surface, but the layering is difficult to distinguish in TEM photo (d).

Table IV shows the composition ratio (N_O/N_{Sn}), the atom number per unit volume (N), and the porosity (P) calculated by RUMP simulation from the RBS spectra in Fig. 7. The composition ratio calculated from RBS has a higher value than that calculated from XPS data. The reason may be as follows; XPS is a surface analysis and the oxygen on the surface layer is removed by Ar-ion sputtering, so, the effect of oxygen absorbed on surface is excluded. But RBS is a volume analysis and there is no ion cleaning process like Ar sputtering; also, the Si substrate has oxygen in a native oxide layer as shown in the TEM images. Thus the RBS analysis, which includes the contributions of oxygen absorbed or trapped in pores during ion beam assisted deposition, shows a higher composition ratio than that found by XPS analysis.

The composition ratio calculated by RBS increased with ion energy in a different manner than that derived from the results of XPS, presumably due to an increase of the porosity in the films. The atomic density of the film (*b*) is $7.917\times 10^{22}\,\#/cm^3$, which is the most dense film, and the closest to the density of SnO_2 single crystal ($8.3916\times 10^{22}\,\#/cm^3$). When the irradiated ion energy increased, the atomic density decreased. In general, a lot of research reports that when the ion bombardment energy increases, the atomic packing density increases, but then, decreases above some critical ion energy.[40] In our study, it is theorized that a great deal of oxygen is trapped inside the films, and the porosity increases with increasing ions/atom arrival ratio.

D. Optical and electrical properties (Derivation of formula for atomic force)

Figure 8 shows the optical transmittance spectra in the wavelength range 200–1200 nm for the BK7 bare glass and as-grown tin oxide films on the glass. From the transmittance curves, all of the as-grown films have very low optical absorption in the visible region. Film (*a*) had high absorption in the short wavelength region. With increasing ion beam energy, in films (*b*)–(*d*), the transmittance in the short wavelength region increased, so that the optical band gaps are equal to or higher than that of BK7 glass because the transmittance curves in the band edge region overlap with that of bare glass.

The optical constants of the tin oxide thin films were calculated by the envelope method[41,42] from the transmittance data in Fig. 8. The envelope method can determine the optical constants of a thin-film from measurement of alone optical transmittance when the film has a low absorption coefficient and optimal thickness. The maximum and minimum transmittances appear when optical thickness of a film is a multiple of quarter and half wavelength, so it can be used to calculate a refractive index (n), an extinction coefficient (k), and a film thickness (d) from envelope curves at maximum and minimum transmittance, respectively.

The dispersion relation of the refractive index as a function of wavelength calculated by the envelope method are shown in Fig. 9. The refractive index decreased with increasing ion beam energy. The film (*a*) grown by low ion energy has a higher refractive index than that of bulk SnO_2. The reason for this might be that the composition ratio is 1.51 with a mixture phase of SnO and SnO_2. The refractive index of stoichiometric film (*b*) is similar to that of bulk SnO_2. The refractive index of films (*b*)–(*d*) decreased with increasing ion beam energy. This reason might be closely associated with the increasing porosity. The porosities calculated from the refractive index are listed in Table IV. The values differed only 5% from the porosity determined from the RBS analysis, and showed a similar tendency as a function of ion beam energy.

The Cauchy equation[43] represents a normal dispersion relation for refractive index, which is written as Eq. (1).

$$n(\lambda)=A+B/\lambda^2+C/\lambda^4, \tag{1}$$

where the capitals A, B, and C are constants, determined from characteristics of a material. This equation fits the data precisely in the visible wavelength range. The solid lines in Fig. 9 are curve fittings by using the Cauchy equation which concurs well with Eq. (1), and the obtained constants are listed in Table V. In Eq. (1), generally, because the third

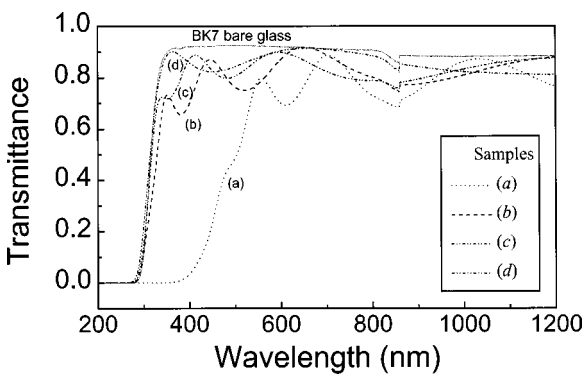

FIG. 8. Spectrophotometric transmittances measured in the wavelength range of 200 to 1200 nm for BK7 bare glass and as-deposited tin-oxide films grown on BK7 glass by R-IAD.

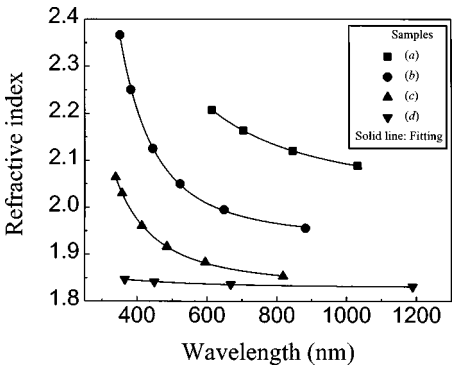

FIG. 9. Dispersion of refraction index n of R-IAD tin-oxide films on BK7 glass.

term is small, a dispersion relation equation can be fully expressed with only two terms. This equation is

$$n = A + B/\lambda^2. \tag{2}$$

The dispersion relation is obtained by differentiation of Eq. (2), which is as follows:

$$dn/d\lambda = -2B/\lambda^3. \tag{3}$$

From Eq. (3), the dispersion is approximately in inverse proportion ratio to the cube of the wavelength, and the constant B represents the degree of dispersion. In Table V, the constant B decreased with increasing ion beam energy. That is, it means that degree of the dispersion decreases, which translates to a decrease in aberration, a useful characteristic for optical applications. The physical meaning of the dispersion is the wavelength dependent variation of light velocity in a medium. Sellmeier has expressed this relationship in the following equation.[44]

$$n^2 = 1 + \frac{D\lambda^2}{\lambda^2 - \lambda_0^2}, \tag{4}$$

where D is a constant, λ is the incident wavelength, and λ_0 is the native vibrational wavelength of the material. Eq. (4) can be expanded as follows:

$$n = A + \frac{D\lambda_0^2}{2(1+D)^{1/2}}\frac{1}{\lambda^2} + \frac{(D\lambda_0^2)^2}{8(1+D)^{3/2}}\frac{1}{\lambda^4} + \cdots. \tag{5}$$

By comparing with the coefficients of Eqs. (1) and (5),

$$B = \frac{D\lambda_0^2}{2(1+D)^{1/2}}. \tag{6}$$

Thus, the main dispersion coefficient B is proportional to the square of the native vibrational wavelength of a material. Therefore, examining the constants B in Table V, we can correlate an increase in the native vibrational frequency with increasing ion beam energy.

If the elastic coefficient between particles in a substance is K_b, the native angular frequency is

$$\omega_0 = \sqrt{k_b/m}, \tag{7}$$

where m is the mass of the particle. If the particles in a same substance all have the same mass, the angular frequency is proportional to the square root of the elastic coefficient. Therefore, an increase of the native natural frequency means an increase of the elastic coefficient between particles. This increase of elastic coefficient derives from an increase of the bonding force between particles. In Fig. 2, d spacings of the films are seen to decrease with increasing ion beam energy, which verifies the above hypothesis. In order to estimate the force exerted by the elastic force in a film, using Eq. (6), Eq. (7), $\omega = 2\pi\nu_0$, and $\lambda_0\nu_0 = v$, we obtain an equation

$$k_b \propto 1/B, \tag{8}$$

where v is the velocity of light in medium. The elastic force due to lattice displacement is

$$F = -k_b \cdot l, \tag{9}$$

where l is a lattice displacement. From Eqs. (8) and (9),

$$F \propto -l/B. \tag{10}$$

The calculated values of Eq. (10) were listed in Table V. The positive and negative signs mean tensile and compressive force, respectively. Film (c) has the lowest stress, while film (d) has a five times higher stress than film (c) but has a low dispersion.

Figure 10 represents experimental and calculated refractive indices obtained from the Cauchy coefficients at 550 nm. The values show good agreement. The refractive index varies from high to low value with increasing ion energy. The refractive index of film (b) is similar to that of bulk SnO_2. The experimental results are very consistent with the calculated refractive index in films with low absorption [films (b)–(d)].

The extinction coefficient (k) as a function wavelength are shown in Fig. 11. The k values of tin oxide films are on the order of 10^{-2}, much smaller than the refractive index, so the

TABLE V. Cauchy coefficients obtained by curve fitting of refractive indices and thickness of films calculated from transmittance.

Samples	A	B (nm^2)	C (nm^4)	$-l/B$ ($\times 10^{-7}$)(nm^{-1})	n (at 550 nm)	Thickness (nm)
Film (a)	2.02328	69773	-7.291×10^7		2.2531	487.04±0.51
Film (b)	1.93204	14024	4.837×10^9	+1.6187	2.0313	325.22±3.11
Film (c)	1.82983	13974	1.464×10^9	−0.4079	1.8920	316.27±0.18
Film (d)	1.82899	3015	-9.760×10^7	−2.1559	1.8379	182.27±0.55

*Cauchy equation; $n(\lambda) = A + B/\lambda^2 + C/\lambda^4$.

*The l is a lattice displacement.

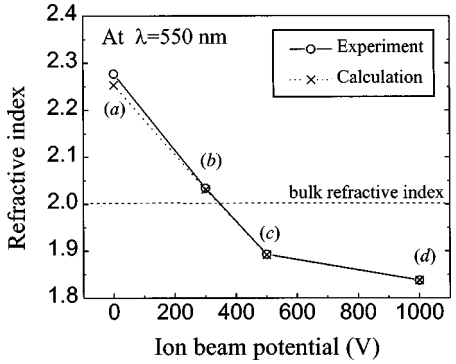

FIG. 10. Refractive index n at 550 nm wavelength of R-IAD tin-oxide films on BK7 glass.

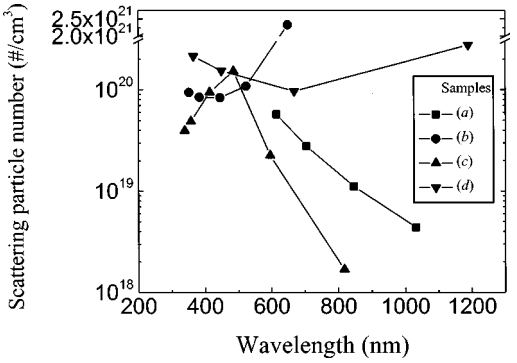

FIG. 12. Number of scattering particles as a function of wavelength of R-IAD tin-oxide films on BK7 glass.

optical constants obtained from our tin oxide films can be trusted because the envelope method is well right when the film has a low k.

The absorption coefficient of light in a substance is expressed as $\alpha=\alpha_a+\alpha_s$, where α_a is the native absorption coefficient of a substance and α_s is the absorption coefficient due to scattering. Since SnO_2 is well known to be a low-absorption material, we can assume that the absorption due to scattering effects dominates.[45] The scattering by a particle that is very small in comparison with the wavelength of light is termed Rayleigh scattering, and is expressed as $\alpha_s=C/\lambda^4$. From the relation that the intensity of scattering is proportional to the square of the volume of the scattering particle and to the incident intensity, we can deduce Eq. (11).[44]

$$n-1=\frac{\lambda^2}{2\pi}\sqrt{\alpha_s N}, \tag{11}$$

where N is the number of scattering particles per unit area. By using the equation relating the absorption and extinction coefficients,

$$\alpha_s=4\pi k_s/\lambda. \tag{12}$$

Equation (11) can be rewritten as

$$k_s=\frac{\pi(n-1)^2}{N\lambda^3}. \tag{13}$$

Finally, we can calculate the number of scattering particles, from a supposition of that n has no dependence on wavelength. Eq. (13) includes Rayleigh's law of scattering. But, Rayleigh's law is not consistent with the data in Fig. 11. In a tin oxide thin film, the scattering derives mainly from three mechanisms: impurities, oxygen pores, and grain boundaries.[45] Equation (13) assumes scattering by particles, which are very small in comparison with the incident wavelength. Since small impurity particles and oxygen pores have very small sizes, Eq. (13) is applicable to these scattering centers. But because the grain size is larger than impurities or pores, scattering grain boundaries must be accounted for specially. Namely, wavelengths longer than the particle size are scattered less strongly than shorter wavelengths. So, if the size of the grain boundary is not smaller than the incident wavelength, especially, when the sizes of the grain boundaries are on the order of $\frac{1}{2}$, $\frac{1}{4}$, $\frac{1}{8}$, and $\frac{1}{16}$ of the wavelength, the scattering is strong. For example, in the case of film (*c*), in Fig. 4, the size of the large masses of grains is about 50 nm, so since the 400 and 800 nm wavelengths are approximately 8 and 16 times the particle size, respectively, the extinction coefficient will be increased near these wavelengths. These results are shown in Fig. 11. Film (*b*) exhibited a higher extinction coefficient than the Rayleigh scattering in the short wavelength range near 480 nm, which is 16 times the grain mass size of about 30 nm. Film (*d*) has clusters similar in size to those in film (*b*) and has more indistinct grain boundaries than film (*b*), and we observe a slight higher extinction coefficient than that contributed by Rayleigh scattering. This result agrees well with the nature of the grain boundaries observed in the SEM analyses. In the SEM image of film (*a*), the grain boundaries are not spherical and the size appears to be about 50–70 nm, which agrees with the observation that the extinction coefficient is increased at 1000 nm, approximately 16 times the grain size. The case of a particle size smaller than $\frac{1}{16}$ wavelength might fall in the category of Rayleigh scattering by small particles, i.e., scattering characteristic of the grain size (about 7–11 nm) and surface roughness (about 1–4 nm) shown in Table II is not observed in Fig. 11.

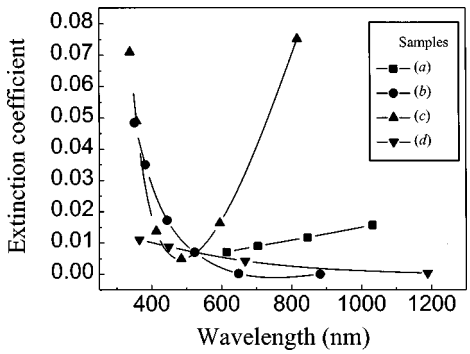

FIG. 11. Extinction coefficient k as a function of wavelength of R-IAD tin oxide films on BK7 glass.

Figure 12 shows the number of scattering particles detected at each wavelength calculated using Eq. (13). The number of scattering particles is estimated to be 10^{18} to 10^{21} per unit volume. The case of 10^{20} particle per unit volume corresponds to one scattering particle per 10^3 atoms, since the atom density of bulk SnO_2 is 8.3916×10^{22} atoms/cm^3. The decrease of scattering particles at some wavelengths ap-

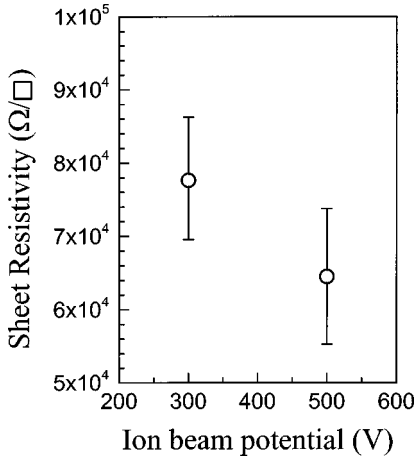

FIG. 13. Sheet resistivities of tin oxide films on BK7 glass substrates.

pears to be due to scattering by large particles, such as grains, massed clusters or grain boundaries.

The sheet resistivities of tin-oxide thin films deposited on glass substrates are shown in Fig. 13. The sheet resistivities of films (*b*) and (*c*) are 7.76×10^4 and $6.45\times10^4\,\Omega/\square$, respectively. But, that of films (*a*) and (*d*) were out of measurement limit. The result is presumed upon that the electrical property of the films is related with the composition ratio and the film thickness. That is, the film (*a*) with mixture phase (SnO and SnO_2) has a low composition ratio ($N_O/N_{Sn}=1.51$) as shown in Fig. 6 and Table III, the film (*d*) has thinner thickness than other films as shown in Table V and SEM image of Fig. 4. The measurement range of used four-point probe is $\sim10^5\,\Omega/\square$, also.

IV. CONCLUSIONS

Tin oxide films were deposited on glass, amorphous-SiO_2/Si (100), and Si (100) substrates using oxygen ion beams of various energies of at room temperature and a working pressure of 8×10^{-5} Torr. The structure, chemical states, and optical properties of the as-grown films were studied and the summarized results are as follows:

A buffer layer of amorphous tin oxide was grown at the interface between the substrate and the film, followed by crystalline grains on top of this buffer layer. The crystalline grains were arranged in large spherical clusters, and these clusters directly affected surface roughness. All films exhibited an amorphous interface between crystalline grains, and had no crystalline defects in the small crystalline grains. Film (*b*) showed the densest structure. Films (*a*) and (*b*) exhibited a composition ratio, which decreased slightly near the film surface, while films (*c*) and (*d*) showed the opposite trend. All films were inhomogeneous tin-oxide thin films. The interfaces between the substrates and the films were sharp.

The effects by increasing of oxygen ion energy lead to the following conclusions.

(1) The crystal structure changed, from amorphous→(101) →(002) textures of rutile SnO_2.
(2) The stress of films was changed from compressive to tensile stress.
(3) The crystallinity of films increased.
(4) Film (*a*) deposited at low energy had unclear grain boundaries. The massed cluster size increased from 30 to 50 nm in the case of films (*b*) and (*c*), and decreased to 25 nm in film (*d*) deposited at very high energy.
(5) Film (*a*) had a mixed phase of SnO and SnO_2. Films (*b*) and (*c*) were stoichiometric SnO_2 films and film (*d*) was close to stoichiometric.
(6) The density of films decreased, and the porosity and oxygen content trapped in the films increased.

Film (*d*) is estimated to be the best optical film, because it was observed to have the lowest dispersion for the refractive index and extinction coefficient. Film (*c*) had the lowest stress. Film (*b*) showed the lowest porosity (about 6%) and had a refractive index similar to that of bulk SnO_2. Film (*a*) was an amorphous mixture of SnO and SnO_2. All prepared tin oxide thin films showed low optical absorption, and the number of scattering particle in the visible wavelength region is observed to be about $10^{20}\#/cm^3$. The degree of the dispersion of the refractive index and extinction coefficient decreased with increasing ion energy. A formula for the atomic bonding force was derived, and the atomic bonding force was found to increase with increasing ion energy, which leads to a decrease in dispersion. The stress of films was changed from compressive to tensile stress with increasing ion energy. A low oxygen: tin ratio was found to increase the refractive index and absorption. The refractive index of films was closely related to the porosity. The main source of scattering was found to be clusters of massed grains. The electric property is presumed to relate with atomic bonding degree.

[1] S. Semancik and T. B. Fryberger, Sens. Actuators B **1**, 97 (1990).
[2] Y. S. He, J. C. Campbell, R. C. Murphy, M. F. Arendt, and J. S. Swinnea, J. Mater. Res. **8**, 3131 (1993).
[3] B. Stierna and C. G. Granqvist, Appl. Opt. **29**, 447 (1990).
[4] A. K. Ghosh, C. Fishman, and T. Feng, J. Appl. Phys. **49**, 3490 (1978).
[5] W. Dazhi, W. Shulin, C. Jun, Z. Suyuan, and L. Fangqing, Phys. Rev. B **49**, 282 (1994).
[6] J. S. Marifacier, L. Szepessy, J. F. Bresse, M. Perotin, and R. Stuck, Mater. Res. Bull. **14**, 109 (1979).
[7] J. S. Maudes and T. Rodrìguez, Thin Solid Films **69**, 183 (1980).
[8] E. Giani and R. Kelly, J. Electrochem. Soc. **121**, 394 (1974).
[9] J. R. Bosnell and R. Waghtone, Thin Solid Films **15**, 141 (1973).
[10] T. Susuki, T. Yamazaki, H. Yoshioka, and K. Hikichi, J. Mater. Sci. **23**, 145 (1988).
[11] S. S. Park and J. D. Mackenzie, Thin Solid Films **258**, 268 (1995).
[12] R. N. Ghostagore, J. Electrochem. Soc. **125**, 110 (1978).
[13] K. H. Kim and T. S. Park, J. Korean Phys. Soc. **18**, 124 (1985).
[14] J. C. Manifacier, M. de Murcia, and J. P. Fillard, Thin Solid Films

41, 127 (1977).
[15] D. W. Lane, J. A. Coath, and H. S. Beldon, Thin Solid Films **221**, 262 (1992).
[16] C. A. Vincent, J. Electrochem. Soc. **119**, 515 (1972).
[17] S. Samson and C. G. Fonstad, J. Appl. Phys. **44**, 4618 (1973).
[18] S. K. Koh, S. K. Song, W. K. Choi, and H.-J. Jung, Rev. Sci. Instrum. **66**, 5379 (1995).
[19] S. K. Song, W. K. Choi, H. K. Baek, H.-J. Jung, and S. K. Koh, J. Korean Appl. Phys. **9**, 246 (1996).
[20] J. J. Cuomo, S. M. Rossnagel, and H. R. Kaufman, *Handbook of Ion Beam Processing Technology* (Noyes, Park Ridge, NJ, 1989), p. 194.
[21] Z. M. Jarzebski, J. Electrochem. Soc. **123**, 199 (1976).
[22] E. Shanthi, V. Dutta, A. Baneriee, and K. L. Chopra, J. Appl. Phys. **51**, 6243 (1981).
[23] G. N. Advani, A. G. Jordan, and P. K. Weiss, Mater. Sci. Eng. **4** (1979).
[24] T. J. Coutts, X. Liand, and T. A. Cessert, IEEE Electron Device Lett. **26**, 660 (1990).
[25] J. Melsheimer and D. Ziegler, Thin Solid Films **129**, 35 (1985).
[26] J. Melsheimer and D. Ziegler, Thin Solid Films **110**, 71 (1983).
[27] J. Zemel, Thin Solid Films **163**, 189 (1988).
[28] W. K. Choi, H. J. Jung, and S. K. Koh, J. Vac. Sci. Technol. **14**, 359 (1996).
[29] S.-K. Song, W.-K. Choi, J.-S. Cho, H.-J. Jung, D. Choi, J.-Y. Lee, H.-K. Baik, and S.-K. Koh, Jpn. J. Appl. Phys., Part 1 **36**, 2281 (1997).
[30] H. R. Kaufman, *Operation of Broad-Beam Source* (Commonwealth Scientific, Alexandria, 1987), p. 133.
[31] L. A. Arzimovich, *Elementary Plasma Physics* (Blaisdell, Waltham, 1965), p. 90.
[32] B. D. Cullity, *Elements of X-ray Diffraction* 2nd ed. (Addison-Wesley, Torrance, CA, 1978), p. 284.
[33] J. W. Edington, *3 Interpretation of Transmission Electron Micrographs* (PHILIPS Pub., Eindhoven, 1975), p. 80.
[34] P. Grosse, F. J. Schmitte, G. Frank, and H. Kostlin, Thin Solid Films **90**, 309 (1982).
[35] E. Krikorian and R. J. Sneed, Astrophys. Space Sci. **65**, 129 (1979).
[36] R. O. Ansell, T. Dickinson, A. F. Povey, and P. M. A. Sherwood, J. Electrochem. Soc. **124**, 1360 (1977).
[37] S. M. Rossnagel, J. J. Cuomo, and W. D. Westwood, *Handbook of Plasma Processing Technology* (Noyes, Park Ridge, NJ, 1990), p. 91.
[38] J. Nowotny and L.-C. Dufour, *Surface and Near-Surface Chemistry of Oxide Materials* (Elsevier, Amsterdam, 1988), p. 137.
[39] A. W. C. Lin, N. R. Armstrong, and T. Kuwana, Anal. Chem. **49**, 1228 (1977).
[40] J. J. Cuomo, S. M. Rossnagel, and H. R. Kaufman, *Handbook of Ion Beam Processing Technology* (Ref. 20), p. 265.
[41] J. C. Manifacier, J. Gasiot, and J. P. Fillard, J. Phys. E **5**, 1002 (1976).
[42] H. A. Mecleod, *Thin Films Optical Filter*, 2nd edition (Hilger, Bristol, 1986).
[43] F. R. Flory, *Thin Films for Optical Systems* (Dekker, New York, 1995), p. 280.
[44] F. A. Jenkins and H. E. White, *Fundamentals of Optics*, 4th edition (McGraw-Hill, Seoul, Korea, 1984), p. 471 and 482.
[45] L. Meng and M. P. Santos, Thin Solid Films **237**, 112 (1994).